

Supplementary Materials for

Strong Ground Motion Prediction Using Virtual Earthquakes

M. A. Denolle,* E. M. Dunham, G. A. Prieto, G. C. Beroza

*Corresponding author. E-mail: mdenolle@stanford.edu

Published 24 January 2014, *Science* **343**, 399 (2014)

DOI: [10.1126/science.1245678](https://doi.org/10.1126/science.1245678)

This PDF file includes

Materials and Methods

Figs. S1 to S7

References

Materials and Methods

To construct the ground motion for large earthquakes (Fig. S1), we introduce the extended Virtual Earthquake Approach (VEA), which is a generalization of the point source VEA (21). We use the convention $\hat{F}(\omega)$ to refer to the Fourier transform of $f(t)$,

and use $\hat{F}(\omega) = \int_{-\infty}^{\infty} f(t)e^{i\omega t} dt$ as convention for the Fourier transform, and

$f(t) = \int_{-\infty}^{\infty} \hat{F}(\omega)e^{-i\omega t} d\omega$ for the inverse transform. We first compute all components of the

Green's tensor G_{ij} in frequency domain with the ambient seismic velocity v_j recorded at a virtual source at surface location $\vec{\xi}' = (x_1', x_2')$ and the velocity v_i recorded at a receiver located at $\vec{\xi} = (x_1, x_2)$,

$$\hat{G}_{ij}(\vec{\xi}', \vec{\xi}, \omega) = A \left\langle \frac{\hat{v}_i(\vec{\xi}, \omega) \hat{v}_j^*(\vec{\xi}', \omega)}{\left\| \hat{v}_j^*(\vec{\xi}', \omega) \right\|^2} \right\rangle, \quad (1)$$

where the operator $\langle \rangle$ denotes stacking over time, and $\langle \rangle$ denotes smoothing over the virtual source spectrum (in our case a 3 mHz running average) to stabilize the deconvolution. We select a normalization factor A to match observed amplitudes because we recover relative, rather than absolute, amplitudes. We transform the Green tensor from North-East-down into radial-transverse-down coordinates, and determine the excitation using the radial and down components for Rayleigh waves and the transverse component for Love waves, thereby neglecting the effect of surface-wave refraction and multi-pathing on excitation. We recover the ambient seismic field Green's functions over the period range of 3-10 s, where the ambient seismic field has the largest amplitudes from the ocean wave excitation. Because the cross-correlation contains positive and negative lags, we only consider the side of the Green's function that has the strongest signal-to-noise ratio, and calibrate the amplitudes using that side of the Green's function.

If may be possible to recover overtones, body waves, or reflected phases from correlation of the ambient seismic field (28–31); however, we appear to recover only the fundamental surface-wave mode (Fig. S1). We correct each surface-to-surface Green's tensor using analytical expressions derived under the assumption that elastic properties vary solely with depth. With this approximation, the Rayleigh- and Love-wave displacement spectrum from a point moment tensor source $M(t)$ at horizontal position $\vec{\xi}'$ and depth $x_3' = h$ are in the far-field limit $\vec{\xi} = (x_1, x_2)$,

$$\hat{U}_T(\vec{\xi}, \omega) = \frac{1}{l_1(\vec{\xi}', 0, \omega)} \left[-ik_L(\omega) \hat{M}_{TR}(\omega) l_1(\vec{\xi}', h, \omega) + \hat{M}_{TD}(\omega) l_1'(\vec{\xi}', h, \omega) \right] \hat{G}_{TT}(\vec{\xi}', \vec{\xi}, \omega), \quad (1)$$

$$\hat{U}_R(\vec{\xi}, \omega) = \frac{1}{r_1(\vec{\xi}', 0, \omega)} \left[-ik_R \hat{M}_{RR}(\omega) r_1(\vec{\xi}', h, \omega) + \hat{M}_{RD}(\omega) l_1'(\vec{\xi}', h, \omega) \right] \hat{G}_{RR}(\vec{\xi}', \vec{\xi}, \omega) + \\ \frac{1}{r_2(\vec{\xi}', 0, \omega)} \left[-ik_R \hat{M}_{DR}(\omega) r_1(\vec{\xi}', h, \omega) + \hat{M}_{DD}(\omega) l_1'(\vec{\xi}', h, \omega) \right] \hat{G}_{DR}(\vec{\xi}', \vec{\xi}, \omega), \quad (2)$$

$$\hat{U}_D(\vec{\xi}, \omega) = \frac{1}{r_1(\vec{\xi}', 0, \omega)} \left[-ik_R \hat{M}_{RR}(\omega) r_1(\vec{\xi}', h, \omega) + \hat{M}_{RD}(\omega) l_1'(\vec{\xi}', h, \omega) \right] \hat{G}_{RD}(\vec{\xi}', \vec{\xi}, \omega) + \\ \frac{1}{r_2(\vec{\xi}', 0, \omega)} \left[-ik_R \hat{M}_{DR}(\omega) r_1(\vec{\xi}', h, \omega) + \hat{M}_{DD}(\omega) l_1'(\vec{\xi}', h, \omega) \right] \hat{G}_{DD}(\vec{\xi}', \vec{\xi}, \omega), \quad (3)$$

where $k_L(\omega)$, $k_R(\omega)$ are the Love- and Rayleigh-wave wavenumbers, $l_1(\vec{\xi}', x_3, \omega)$, $r_1(\vec{\xi}', x_3, \omega)$, $r_2(\vec{\xi}', x_3, \omega)$ are the Love- and Rayleigh-wave displacement eigenfunctions, and $\hat{G}_{DD}(\vec{\xi}', \vec{\xi}, \omega)$, $\hat{G}_{DR}(\vec{\xi}', \vec{\xi}, \omega)$, $\hat{G}_{RD}(\vec{\xi}', \vec{\xi}, \omega)$, $\hat{G}_{RR}(\vec{\xi}', \vec{\xi}, \omega)$, $\hat{G}_{TT}(\vec{\xi}', \vec{\xi}, \omega)$ are the surface-to-surface ambient seismic field Green's functions. The dependence of the wavenumbers and eigenfunctions on horizontal location x_i' enters solely through the selection of the depth-dependent structure. We obtain the surface-wave eigenfunctions (Fig. S3b) using the elastic wavespeed and density profiles extracted from the Southern California Earthquake Center Community Velocity Model-S4 (23–24), and solve the surface-wave eigenproblem using the Generalized Eigenproblem Spectral Collocation method (25).

We reconstruct the seismograms from the large earthquake using the representation theorem (22), as follows. First, we discretize the fault into sub-faults, and compute the VEA waveforms by treating each sub-fault as a point source. Next, we convolve the corrected waveforms for the starting time and the source time function of each point source. Finally, we sum the contribution of all point sources (Fig. S3d). By summing the contributions of sub-faults, we allow for a general representation of directivity effects without resorting to, for example, a local line-source approximation. Because the SAVELA seismic stations are approximately 5 km apart (Fig. 1), we approximate the Green's function for point sources located between two station sources by introducing a time shift using the phase velocity estimated from the surface-wave eigen problem (21,25). We do not consider the near-field measurements for receivers that are located within 30 km of the fault.

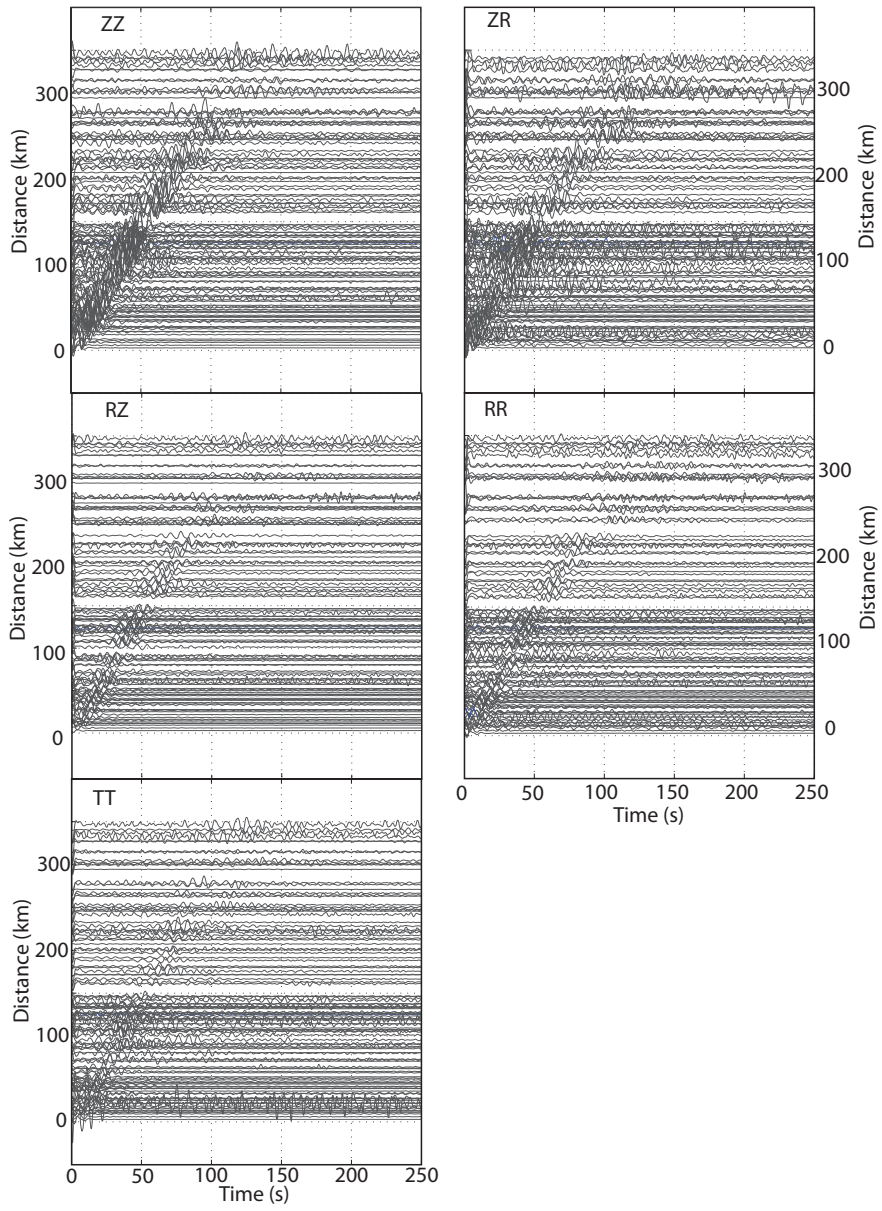


Fig. S1.

Surface-wave impulse responses. One-sided correlation functions with source located on the San Andreas Fault (STA07) and receivers located in Los Angeles Basin. The fundamental mode of Rayleigh waves dominates the ZZ, ZR, RZ and RR components while the fundamental mode of Love waves dominates the TT component.

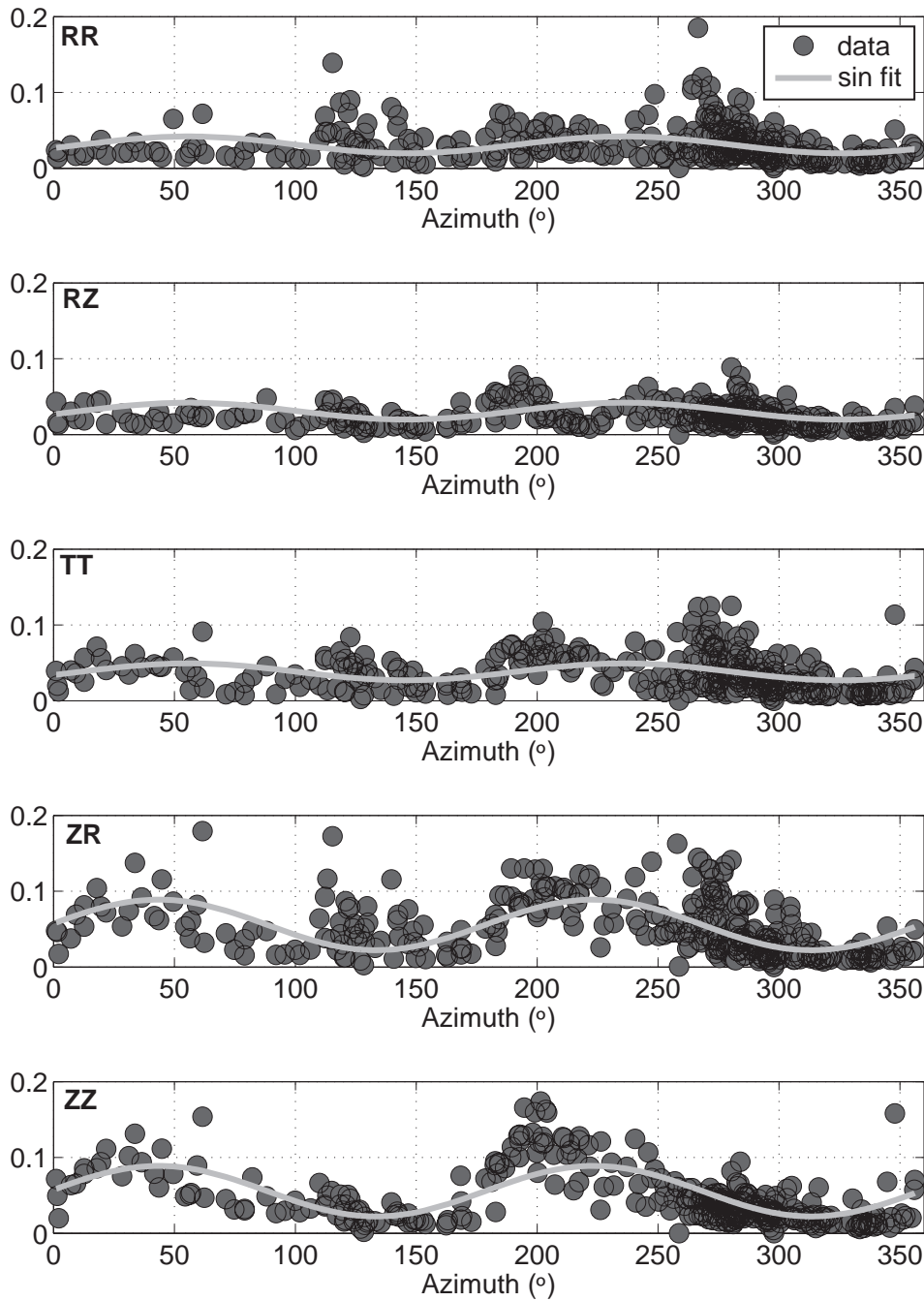


Fig. S2.

Effect of directionality of the ambient seismic field on surface-wave Green's functions amplitudes. Peak amplitudes of the Green's functions (one sided) with respect of azimuth from two permanent stations DEV and MGE used in amplitude calibration. To respect each source mechanism, we find the best matching sinusoidal functions that explain the Love waves (TT component), the radial Rayleigh waves (RR and RZ components), and the vertical Rayleigh waves (ZZ and ZR components).

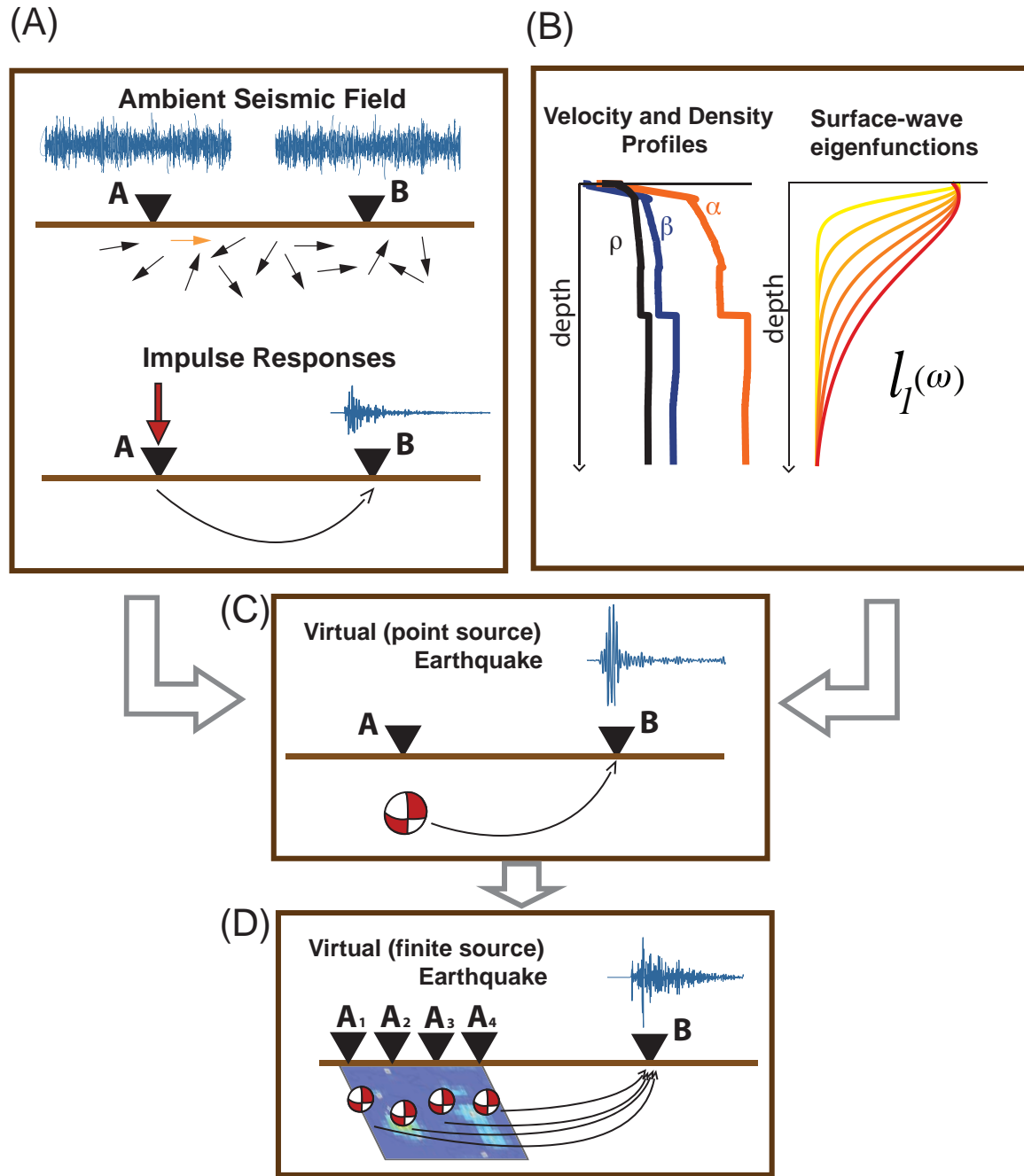


Fig. S3

Flowchart of the extended virtual earthquake approach. (A) Compute the ASF Green's function, (B) estimate the surface-wave excitation, (C) correct for the point source virtual earthquake, and (D) sum the point sources to simulate finite rupture effects.

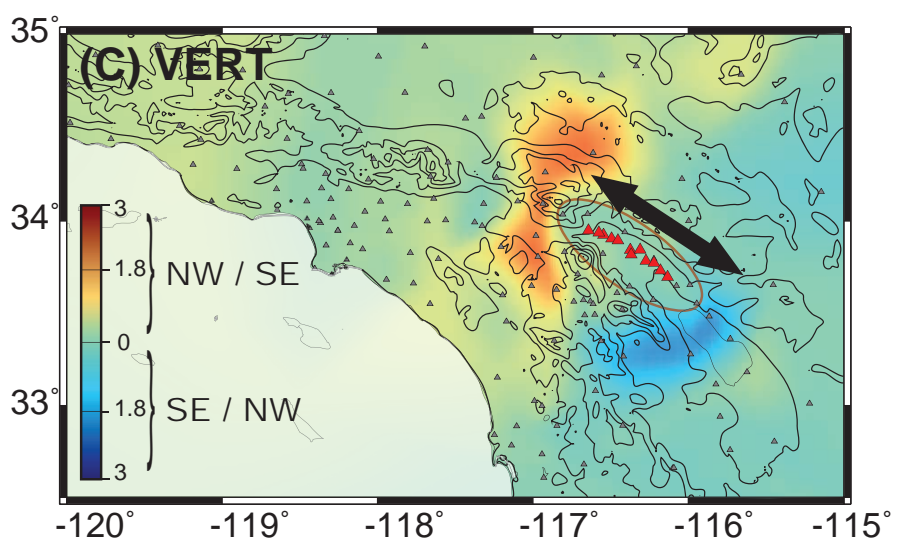
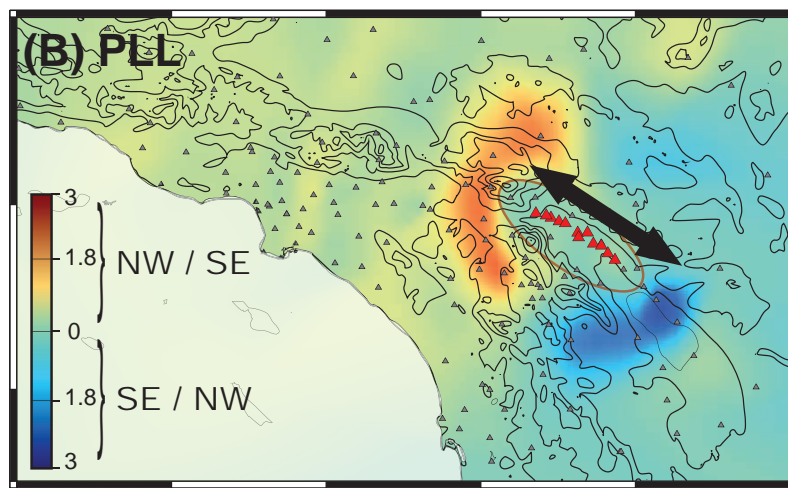
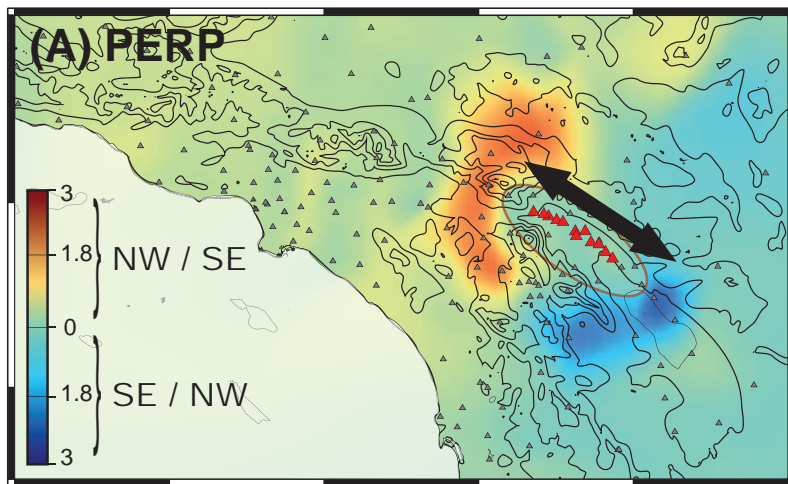


Fig. S4

Source directivity effect on peak ground motion. Ratio of the PGV averaged over all northwestward and southeastward propagating rupture assuming the medium is laterally homogenous with velocity profile under DEV station used as reference. We construct the surface-to-surface Green tensor using equations 7.146 and 7.147 in Chapter 7 of “Quantitative Seismology”, *Aki and Richards* (2002) from each station source to all receivers and implement the VEA correction to estimate the ratio of peak amplitudes for the perpendicular (A), parallel (B), and vertical (C) components. Compared to the 3D case (Fig. 3), we see lesser contrast and extent of the directivity effect between both scenario earthquakes and the dipole-like pattern formed by the directivity of the rupture propagation around the fault zone.

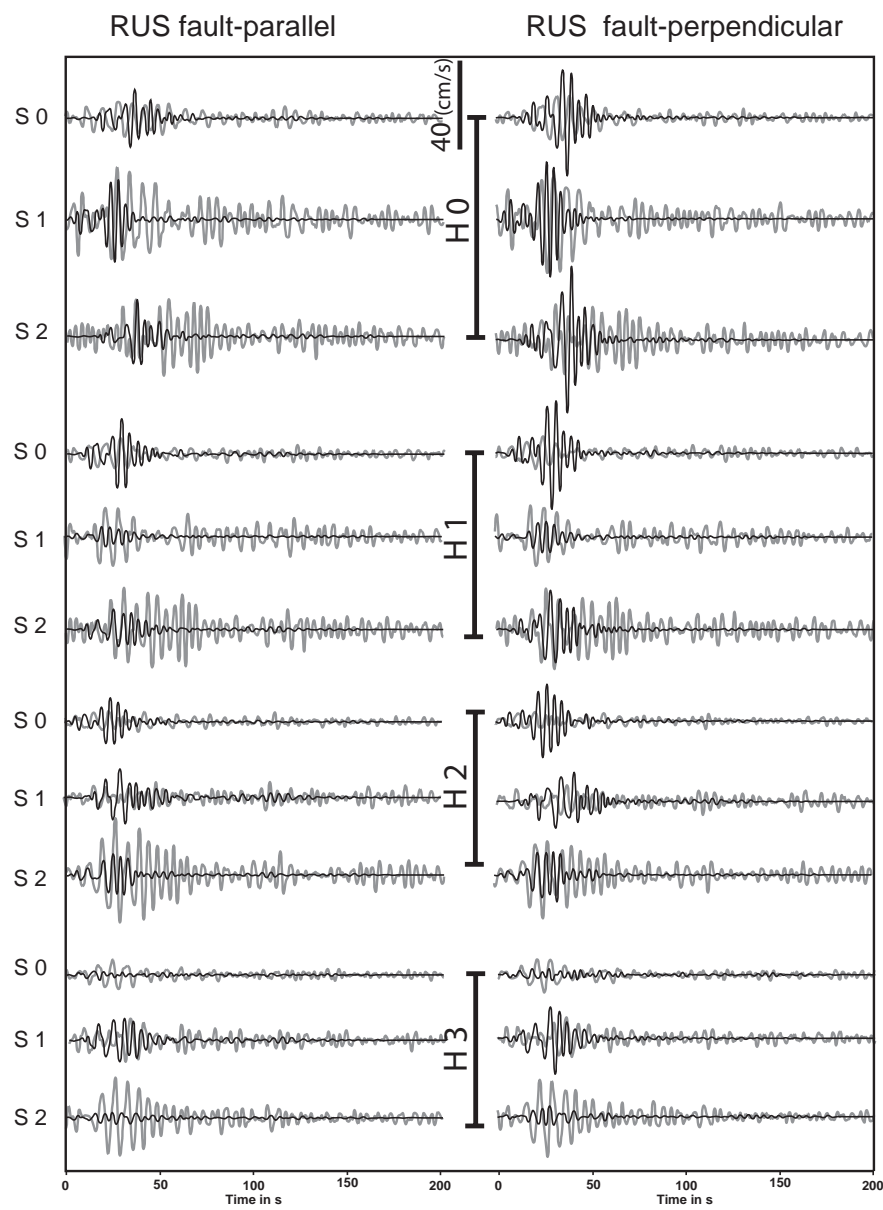


Fig. S5

Waveform comparison between SAVELA and CyberShake. Waveform comparison between SAVELA and CyberShake of the parallel-to-strike component, for NW and SE propagating ruptures at LAF.

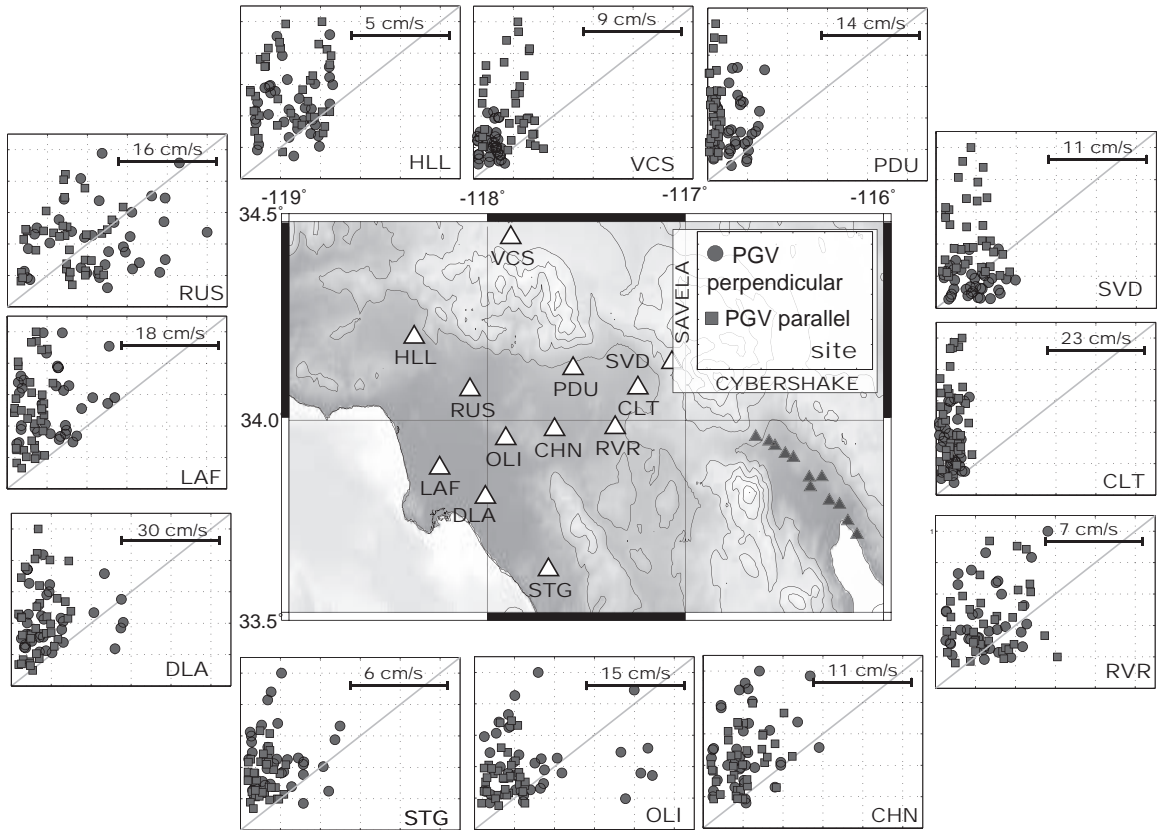


Fig. S6

Horizontal peak ground motion comparison between CyberShake and SAVELA.

Scatter plots of the predicted PGV from CyberShake (x-axis) and SAVELA (y-axis) normalized at each site for a maximal prediction for 36 scenario earthquakes. Gray line is perfect fit, parallel component (squares) and perpendicular components (dots). PGV is scaled on the top right corners.

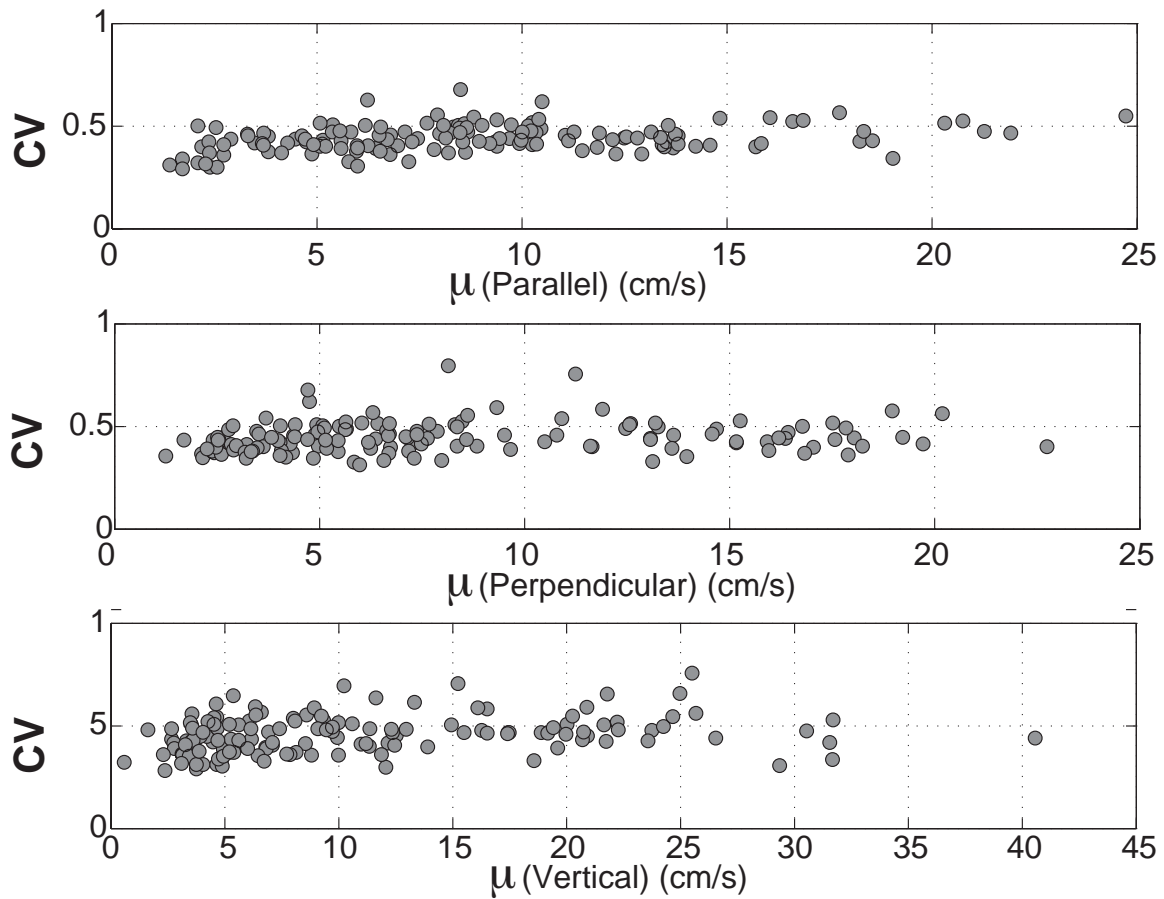


Fig. S7

Relation between mean ground motion and ground motion variability. Coefficient of variation $CV = \sigma/\mu$ where μ is the mean PGV and σ the standard deviation at each station, for the fault-perpendicular (top), fault-parallel (medium) and vertical (bottom) components. The uncertainties grow with the ground motion.

References

1. P.-Y. Bard, M. Campillo, F. J. Chávez-Garcia, F. J. Sánchez-Sesma, The Mexico earthquake of September 19, 1985—A theoretical investigation of large- and small-scale amplification effects in the Mexico City valley. *Earthq. Spectra* **4**, 609–633 (1988).
2. K. B. Olsen, R. J. Archuleta, J. R. Matarese, Three-dimensional simulation of a magnitude 7.75 earthquake on the San Andreas fault. *Science* **270**, 1628–1632 (1995).
3. K. Olsen, S. M. Day, J. B. Minster, Y. Cui, A. Chourasia, M. Faerman, R. Moore, P. Maechling, T. Jordan, Strong shaking in Los Angeles expected from southern San Andreas earthquakes. *Geophys. Res. Lett.* **33**, L07305 (2006).
4. K. B. Olsen, S. M. Day, L. A. Dalguer, J. Mayhew, Y. Cui, J. Zhu, V. M. Cruz-Atienza, D. Roten, P. Maechling, T. Jordan, D. Okaya, A. Chourasia, ShakeOutD: Ground motion estimates using an ensemble of large earthquakes on the southern San Andreas fault with spontaneous rupture propagation. *Geophys. Res. Lett.* **36**, L04303 (2009).
5. K. B. Olsen, Site amplification in the Los Angeles Basin from three-dimensional modeling of ground motion. *Bull. Seismol. Soc. Am.* **90** (6B), S77–S94 (2000).
6. R. Graves, T. Jordan, S. Callaghan, E. Deelman, E. Field, G. Juve, V. Kesselman, P. Maechling, G. Mehta, K. Milner, D. Okaya, P. Small, K. Vahi, CyberShake: A physics-based seismic hazard model for southern California. *Pure Appl. Geophys.* **168**, 367–381 (2011).
7. S. M. Day, D. Roten, K. B. Olsen, Adjoint analysis of the source and path sensitivities of basin-guided waves. *Geophys. J. Int.* **189**, 1103–1124 (2012).
8. K. Aki, Space and time spectra of stationary stochastic waves, with special reference to microtremors. *Bull. Earthq. Res. I. Tokyo* **35**, 415 (1957).
9. J. Claerbout, Synthesis of a layered medium from its acoustic transmission response. *Geophysics* **33**, 264–269 (1968).
10. O. I. Lobkis, R. L. Weaver, On the emergence of the Green's function in the correlations of a diffuse field. *J. Acoust. Soc. Am.* **110**, 3011 (2001).
11. R. L. Weaver, O. I. Lobkis, On the correlation of non-isotropically distributed ballistic scalar diffuse waves. *Geophysics* **71**, S15 (2006).
12. F. J. Sánchez-Sesma, M. Campillo, Retrieval of the Green's function from cross correlation: The canonical elastic problems. *Bull. Seismol. Soc. Am.* **96**, 1182–1191 (2006).
13. M. Campillo, A. Paul, Long-range correlations in the diffuse seismic coda. *Science* **299**, 547–549 (2003).
14. N. M. Shapiro, M. Campillo, Emergence of broadband Rayleigh waves from correlations of the ambient seismic noise. *Geophys. Res. Lett.* **31**, L07614 (2004).

15. K. G. Sabra, P. Gerstoft, P. Roux, W. A. Kuperman, M. C. Fehler, Extracting time-domain Green's function estimates from ambient seismic noise. *Geophys. Res. Lett.* **32**, L03310 (2005).
16. N. M. Shapiro, M. Campillo, L. Stehly, M. H. Ritzwoller, High-resolution surface-wave tomography from ambient seismic noise. *Science* **307**, 1615–1618 (2005).
17. K. Nishida, H. Kawakatsu, K. Obara, Three-dimensional crustal S wave velocity structure in Japan using microseismic data recorded by Hi-net tiltmeters. *J. Geophys. Res.* **113** (B10), B10302 (2008).
18. G. A. Prieto, J. F. Lawrence, G. C. Beroza, Anelastic Earth structure from the coherency of the ambient seismic field. *J. Geophys. Res.* **114** (B7), B07303 (2009).
19. G. A. Prieto, M. Denolle, J. F. Lawrence, G. C. Beroza, On amplitude information carried by the ambient seismic field. *C. R. Geosci.* **343**, 600–614 (2011).
20. G. A. Prieto, G. C. Beroza, earthquake ground motion prediction using the ambient seismic field. *Geophys. Res. Lett.* **35**, L14304 (2008).
21. M. A. Denolle, E. M. Dunham, G. A. Prieto, G. C. Beroza, Ground motion prediction of realistic earthquake sources using the ambient seismic field. *J. Geophys. Res.* **118**, 2102 (2013).
22. R. Burridge, L. Knopoff, Body force equivalents for seismic dislocations. *Bull. Seismol. Soc. Am.* **54**, 1875–1888 (1964).
23. H. Magistrale, S. Day, R. W. Clayton, R. Graves, The SCEC Southern California Reference Three-Dimensional Seismic Velocity Model version 2. *Bull. Seismol. Soc. Am.* **90** (6B), S65–S76 (2000).
24. M. D. Kohler, H. Magistrale, R. W. Clayton, Mantle heterogeneities at the SCEC Reference Three-Dimensional Seismic Velocity Model version 3. *Bull. Seismol. Soc. Am.* **93**, 757–774 (2003).
25. M. A. Denolle, E. M. Dunham, G. C. Beroza, Solving the surface-wave eigenproblem with Chebyshev spectral collocation. *Bull. Seismol. Soc. Am.* **102**, 1214–1223 (2012).
26. L. Stehly, M. Campillo, N. Shapiro, A study of the seismic noise from its long-range correlation properties. *J. Geophys. Res.* **111** (B10), B10306 (2006).
27. M. Guatteri, P. M. Mai, G. C. Beroza, A pseudo-dynamic approximation for dynamic rupture models for strong ground motion prediction. *Bull. Seismol. Soc. Am.* **94**, 2051–2063 (2004).
28. K. W. Campbell, Y. Bozorgnia, Updated near-source ground-motion (attenuation) relations for the horizontal and vertical components of peak ground acceleration and acceleration response spectra. *Bull. Seismol. Soc. Am.* **93**, 314–331 (2003).
29. D. Roten, K. B. Olsen, J. C. Pechmann, Simulations of $M 7$ Earthquakes on the Wasatch Fault, Utah, Part II: Broadband (0–10 Hz) ground motions and nonlinear soil behavior. *Bull. Seismol. Soc. Am.* **102**, 2008–2030 (2012).

30. M. K. Savage, F.-C. Lin, J. Townend, Ambient noise cross-correlation observations of fundamental and higher-mode Rayleigh wave propagation governed by basement resonance. *Geophys. Res. Lett.* **40**, 3556–3561 (2013).
31. Z. Zhan, S. Ni, D. V. Helmberger, R. W. Clayton, Retrieval of Moho-reflected shear wave arrivals from ambient seismic noise. *Geophys. J. Int.* **182**, 408–420 (2010).
32. P. Poli, H. A. Pedersen, M. Campillo, POLENET/LAPNET Working Group, Emergence of body waves from cross-correlation of short period seismic noise. *Geophys. J. Int.* **188**, 549–558 (2012).
33. F.-C. Lin, V. C. Tsai, B. Schmandt, Z. Duputel, Z. Zhan, Extracting seismic core phases with array interferometry. *Geophys. Res. Lett.* **40**, 1049–1053 (2013).